Discrete and Continuous Dynamical Systems - Series S

doi:10.3934/dcdss.2023069

BINARY FLUID FLOW SIMULATIONS WITH FREE ENERGY LATTICE BOLTZMANN METHODS

Stephan Simonis[*1,2], Johannes Nguyen[1,2], Samuel J. Avis[3], Willy Dörfler[1] and Mathias J. Krause[1,2,4]

[1]Institute for Applied and Numerical Mathematics (IANM), Karlsruhe Institute of Technology (KIT), Germany

[2]Lattice Boltzmann Research Group (LBRG), Karlsruhe Institute of Technology (KIT), Germany

[3]Department of Physics, Durham University, United Kingdom

[4]Institute of Mechanical Process Engineering and Mechanics (MVM), Karlsruhe Institute of Technology (KIT), Germany

Abstract. We use free energy lattice Boltzmann methods to simulate shear and extensional flows of a binary fluid in two and three dimensions. To this end, two classical configurations are digitally twinned, namely a parallel-band device for binary shear flow and a four-roller apparatus for binary extensional flow. The free energy lattice Boltzmann method and the test cases are implemented in the open-source parallel C++ framework OpenLB and evaluated for several non-dimensional numbers. Characteristic deformations are captured, where breakup mechanisms occur for critical capillary regimes. Though the known mass leakage for small droplet-domain ratios and large Cahn numbers is observed, suitable mesh sizes show good agreement to analytical predictions and reference results.

1. **Introduction.** Fluid mixture flows are omnipresent in nature and essential to many industrial processes [6]. Taylor [39] proposed machinery to examine the deformations of droplets induced by shear and extensional flow of fluids with two components. In the present article, we refer to the latter as binary fluids. The deformation is governed by the balance of outer forces and surface tension. Once this force balance is in favor of deformation, the droplet will break. Modifying the properties of the system, the breakup process can be adjusted in terms of number and size of resulting droplets. These phenomena are essential in manufacturing processes, for example in order to maximize the efficiency of creating emulsions [5, 41]. For the computer simulation of binary fluid flow several methods have been employed in the past. Due to the intrinsic parallelizability which enables the outsourcing of high performance computing (HPC) machinery, the lattice Boltzmann method (LBM) emerged as an unconventional alternative for multicomponent computational fluid

2020 *Mathematics Subject Classification.* Primary 65M22, 35Q30; Secondary 76D05, 76T99.

Key words and phrases. Lattice Boltzmann methods, free energy model, multicomponent flow, Navier–Stokes equations, Cahn–Hilliard equation.

*Corresponding author: Stephan Simonis.

dynamics (CFD). The popularity of LBM for CFD and beyond has increased significantly [23]. Several data structures are available commercially and open-source. Exemplarily for the latter, the highly parallel C++ framework OpenLB [18] has been successfully used for simulations of various transport processes also on Top500 HPC machines (e.g. [18, 10, 30, 26, 7, 36, 32, 9, 35, 31, 33, 4]). Simulating multiphase and multicomponent flows in LBM is mostly based on phase field models with diffuse interfaces. The interfacial zone brings forth additional physics captured by the Cahn–Hilliard equation (CHE), though in turn upholds the high parallelizability of LBM. Several approaches for the underlying mixture dynamics exist [14], for example the free energy model (FRE) [38, 27]. Tunable physical effects and a top-down configuration of thermodynamics, are advantages of models akin to FRE. Albeit a high potential for numerical simulations, applications with FRE LBM for flows relevant to industrial processes are still rare.

The dynamic effects on an immiscible mixture of two components can be abstracted into shear- and extension-dominated flows. For these two types of dynamic mixture flows, the present work implements and tests the FRE LBM with a simple binary fluid composition (equal density and viscosity). In particular, deformation as well as breakup phenomena are distinctively assessed to determine the models usability for more complex applications. As such, we approve the suitability of the presented FRE LBM for numerically simulating these types of binary fluid flows via digitally twinning classical devices and comparing the results to references.

This paper is structured as follows. Section 2 summarizes the methods, the numerical results are described in Section 3 and Appendix A, and Section 4 draws conclusions and closes the paper.

2. Methodology.

2.1. Target equations.

A weakly compressible, isothermal fluid flow is described via the Navier–Stokes equations (NSE)

$$\partial_t \rho + \partial_\alpha(\rho u_\alpha) = 0, \qquad \text{in } \mathfrak{R}, \quad (1)$$

$$\partial_t(\rho u_\alpha) + \partial_\beta(\rho u_\alpha u_\beta) = \partial_\beta\left[\eta\left(\partial_\alpha u_\beta + \partial_\beta u_\alpha\right) + \nu\partial_\gamma u_\gamma \delta_{\alpha\beta}\right] - \partial_\beta P^{\mathrm{th}}_{\alpha\beta}, \qquad \text{in } \mathfrak{R}, \quad (2)$$

where $\rho\colon \mathfrak{R} \to \mathbb{R}$ denotes the density, $\boldsymbol{u}\colon \mathfrak{R} \to \mathbb{R}^d$ is the fluid velocity, $\eta > 0$ is a dynamic viscosity, the factor $\nu = (\eta_{\mathrm{B}} - 2\eta/3) \geq 0$ contains the bulk viscosity $\eta_{\mathrm{B}} \geq 0$, and $\mathfrak{R} = \Omega \times I$ is the space-time domain with $\Omega \subseteq \mathbb{R}^d$ and $I \subseteq \mathbb{R}^+$, respectively. Here, $\mathbf{P}^{\mathrm{th}}\colon \mathfrak{R} \to \mathbb{R}^{d\times d}$ is the thermodynamic pressure tensor with

$$\mathbf{P}^{\mathrm{th}} = \mathbf{P}^{\mathrm{chem}} + P\mathbf{I}_d. \quad (3)$$

For single phase and single component flow, $\mathbf{P}^{\mathrm{th}}$ reduces to the isotropic pressure $P\mathbf{I}_d$. In case of a multicomponent flow model the corresponding thermodynamics are introduced by the partly anisotropic chemical pressure tensor $\mathbf{P}^{\mathrm{chem}}$ [38, 15].

In the present work, we use

$$\partial_\beta P^{\mathrm{chem}}_{\alpha\beta} = \rho\partial_\alpha\mu_\rho + \phi\partial_\alpha\mu_\phi \quad (4)$$

to model a binary fluid system. Capturing additional physics of the diffuse interface, the Cahn–Hilliard equation (CHE)

$$\partial_t\phi + \boldsymbol{\nabla}\cdot(\phi\boldsymbol{u}) = M_\phi\boldsymbol{\Delta}\mu_\phi, \quad \text{in } \mathfrak{R} \quad (5)$$

is coupled to (2), where $\phi\colon \mathfrak{R} \to \mathbb{R}$ is the order parameter, μ_ρ and μ_ϕ denote the chemical potentials and $M_\phi > 0$ is related to the mobility of the interface. The

latter three quantities are specified further below. Complemented with respective initial and boundary conditions, equations (1), (2), and (5) are to be approximated with a FRE LBM.

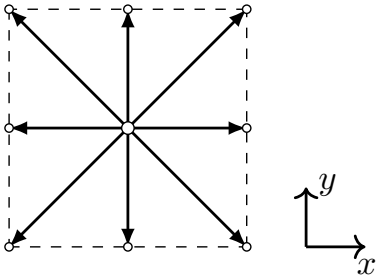

(A) $D2Q9$

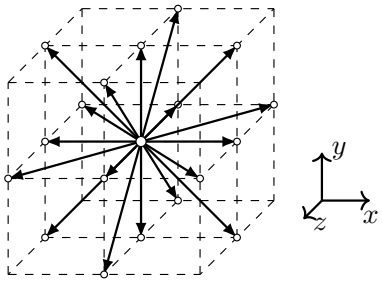

(B) $D3Q19$

FIGURE 1. Discrete velocity sets.

2.2. **Free energy lattice Boltzmann method.** We assume a classical discretization of the phase space and the time domain [20] such that the following derivation is done completely in (dimensionless) lattice units ($\triangle t^{\mathrm{L}} = 1 = \triangle x^{\mathrm{L}}$).

The present LBM is based on the lattice Boltzmann equation (LBE)

$$f_i\left(\boldsymbol{x}+\boldsymbol{c}_i, t+1\right) = f_i\left(\boldsymbol{x}, t\right) + J_i\left(\boldsymbol{x}, t\right) + S_i\left(\boldsymbol{x}, t\right), \tag{6}$$

where $i = 0, 1, \ldots, q-1$ counts the discrete velocities $\boldsymbol{c}_i$ in $DdQq$ and $\boldsymbol{f}\left(\boldsymbol{x}, t\right) = \left(f_i(\boldsymbol{x}, t)\right)_i^{\mathrm{T}}$ denotes the populations in discrete space-time $(\boldsymbol{x}, t) \in (\Omega_h, I_h) \subseteq \mathfrak{R}$ and maps to $\mathbb{R}^q$. The here used velocity stencils are given in Figure 1. The classical Bhatnagar–Gross–Krook (BGK) collision model [2] implements the collision operator

$$\boldsymbol{J}\left(\boldsymbol{x}, t\right) = -\frac{1}{\tau}\left[\boldsymbol{f}\left(\boldsymbol{x}, t\right) - \boldsymbol{f}^{\mathrm{eq}}\left(\boldsymbol{x}, t\right)\right], \tag{7}$$

where $\tau > 0.5$ denotes the relaxation time at which $\boldsymbol{f}$ relaxes towards the equilibrium

$$f_i^{\mathrm{eq}}\left(\boldsymbol{x}, t\right) = w_i \rho\left(\boldsymbol{x}, t\right)\left[1 + \frac{c_{i\alpha} u_\alpha\left(\boldsymbol{x}, t\right)}{c_{\mathrm{s}}^2} + \frac{u_\alpha\left(\boldsymbol{x}, t\right) u_\beta\left(\boldsymbol{x}, t\right)\left(c_{i\alpha} c_{i\beta} - c_{\mathrm{s}}^2 \delta_{\alpha\beta}\right)}{2 c_s^4}\right] \tag{8}$$

with w_i denoting the lattice weights and c_s being the lattice speed of sound. The term $S_i\left(\boldsymbol{x},t\right)$ obeys Guo's forcing scheme [8]

$$S_i\left(\boldsymbol{x},t\right)=\left(1-\frac{1}{2\tau}\right)w_i\left[\frac{\boldsymbol{c}_i-\boldsymbol{u}\left(\boldsymbol{x},t\right)}{c_\mathrm{s}^2}+\frac{\left(\boldsymbol{c}_i\cdot\boldsymbol{u}\left(\boldsymbol{x},t\right)\right)\boldsymbol{c}_i}{c_\mathrm{s}^4}\right]\cdot\boldsymbol{F}\left(\boldsymbol{x},t\right), \tag{9}$$

where $\boldsymbol{F}$ is a force field. The macroscopic flow variables are recovered via the discrete moments of the populations

$$\rho\left(\boldsymbol{x},t\right)=\sum_{i=0}^{q-1}f_i\left(\boldsymbol{x},t\right), \tag{10}$$

$$\rho\left(\boldsymbol{x},t\right)\boldsymbol{u}\left(\boldsymbol{x},t\right)=\sum_{i=0}^{q-1}\boldsymbol{c}_i f_i\left(\boldsymbol{x},t\right)+\frac{1}{2}\boldsymbol{F}\left(\boldsymbol{x},t\right), \tag{11}$$

respectively. As such, we use (6) to approximate the conservative variables in the NSE (1) and (2). Formal Chapman–Enskog expansions are given in [20] and limit consistency is proven force-free in [34]. Both establish the relation

$$\eta=\rho c_s^2\left(\tau-\frac{1}{2}\right) \tag{12}$$

and implicitly $\eta_\mathrm{B}=2\eta/3$. The appropriate body force to recover the divergence of the chemical pressure (4) is defined as the residual

$$\begin{aligned}F_\alpha&=-\partial_\beta(P^\mathrm{th}_{\alpha\beta}-c_\mathrm{s}^2\rho\delta_{\alpha\beta})\\&=-\partial_\beta P^\mathrm{chem}_{\alpha\beta}\\&=-\rho\partial_\alpha\mu_\rho-\phi\partial_\alpha\mu_\phi.\end{aligned} \tag{13}$$

For coupling the approximations of (1), (2) and (5) through the force (13), the thermodynamics can be consistently derived for a binary fluid via the free energy functional [16, 27]

$$\begin{aligned}\Psi=\int_\Omega\Big[&\frac{\kappa_1}{32}(\rho+\phi)^2(\rho+\phi-2)^2+\frac{\alpha^2\kappa_1}{8}(\boldsymbol{\nabla}\rho+\boldsymbol{\nabla}\phi)^2\\&+\frac{\kappa_2}{32}(\rho-\phi)^2(\rho-\phi-2)^2+\frac{\alpha^2\kappa_2}{8}(\boldsymbol{\nabla}\rho-\boldsymbol{\nabla}\phi)^2\Big]\mathrm{d}\boldsymbol{x},\end{aligned} \tag{14}$$

where κ_1, κ_2, and α are tunable parameters for the interface tension, and arguments are neglected where unambiguous. The auxiliary variables ρ and ϕ are defined as

$$\rho=C_1+C_2, \tag{15}$$

$$\phi=C_1-C_2, \tag{16}$$

respectively, where C_1 and C_2 are the concentration fractions of the respective components. The chemical potentials μ_ρ and μ_ϕ are defined as functional derivatives of the free energy

$$\begin{aligned}\mu_\rho=\frac{\delta\Psi}{\delta\rho}=&\frac{\kappa_1}{8}(\rho+\phi)(\rho+\phi-2)(\rho+\phi-1)\\&+\frac{\kappa_2}{8}(\rho-\phi)(\rho-\phi-2)(\rho-\phi-1)\\&+\frac{\alpha^2}{4}\left[(\kappa_1+\kappa_2)(-\boldsymbol{\nabla}^2\rho)+(\kappa_2-\kappa_1)\boldsymbol{\nabla}^2\phi\right]\end{aligned} \tag{17}$$

and

$$\begin{aligned}\mu_\phi = \frac{\delta\Psi}{\delta\phi} =& \frac{\kappa_1}{8}(\rho+\phi)(\rho+\phi-2)(\rho+\phi-1) \\ &- \frac{\kappa_2}{8}(\rho-\phi)(\rho-\phi-2)(\rho-\phi-1) \\ &+ \frac{\alpha^2}{4}\left[(\kappa_1+\kappa_2)(-\boldsymbol{\nabla}^2\phi) + (\kappa_2-\kappa_1)\boldsymbol{\nabla}^2\rho\right], \end{aligned} \tag{18}$$

respectively. The free energy of the system is minimized at equilibrium through the thermodynamic force induced by the chemical pressure. In case of a planar interface, the minimization of the free energy yields a simplified interface solution

$$\phi(x) = \tanh\left(\frac{x}{\xi}\right), \tag{19}$$

where $\xi = 2\alpha$ is the interface width and the bulk components are identified by $\phi = \pm 1$ at $x = \pm\infty$ [22]. For approximating the CHE (5), a second population $g_i(\boldsymbol{x}, t)$ is required such that its zeroth moment yields the order parameter

$$\phi(\boldsymbol{x}, t) = \sum_i g_i(\boldsymbol{x}, t). \tag{20}$$

This population evolves according to a second LBE

$$g_i(\boldsymbol{x} + \boldsymbol{c}_i, t+1) = g_i(\boldsymbol{x}, t) - \frac{1}{\tau_g}\left[g_i(\boldsymbol{x}, t) - g_i^{\mathrm{eq}}(\boldsymbol{x}, t)\right], \tag{21}$$

where $\tau_g > 0.5$. To recover the coupled CHE (5) in the continuum limit [20, 27], the corresponding equilibrium reads

$$\begin{aligned} g_i^{\mathrm{eq}}(\boldsymbol{x}, t) = w_i \Bigg[&\frac{\Gamma_\phi \mu_\phi(\boldsymbol{x}, t)}{c_{\mathrm{s}}^2} + \frac{\phi(\boldsymbol{x}, t)\, c_{i\alpha} u_\alpha(\boldsymbol{x}, t)}{c_{\mathrm{s}}^2} \\ &+ \frac{\phi(\boldsymbol{x}, t)\, u_\alpha(\boldsymbol{x}, t)\, u_\beta(\boldsymbol{x}, t)\left(c_{i\alpha}c_{i\beta} - c_s^2\delta_{\alpha\beta}\right)}{2c_s^4}\Bigg], \end{aligned} \tag{22}$$

if $i \neq 0$, and

$$g_0^{\mathrm{eq}}(\boldsymbol{x}, t) = \phi(\boldsymbol{x}, t) - \sum_{i\neq 0} g_i^{\mathrm{eq}}(\boldsymbol{x}, t), \tag{23}$$

otherwise, where Γ_ϕ relates to the mobility [17]

$$M_\phi = \Gamma_\phi(\tau_g - 0.5). \tag{24}$$

It is to be noted that a flow with three or more components can be realized in a straightforward extension of the equation system $\{(1), (2), (5)\}$, by adding a similarly coupled CHE for each additional order parameter [27] and thus one population for each additional component.

2.3. **Implementation.** The evolution equations for $\boldsymbol{f}$ (6) and $\boldsymbol{g} = (g_i)_i^{\mathrm{T}}$ (21) are split into local collision at $(\boldsymbol{x}, t)$ which computes the post-collision populations $\boldsymbol{f}^\star$ and $\boldsymbol{g}^\star$, respectively, and streaming to evolve

$$\boldsymbol{f}(\boldsymbol{x} + \boldsymbol{c}_i, t+1) = \boldsymbol{f}^\star(\boldsymbol{x}, t) \tag{25}$$

and

$$\boldsymbol{g}(\boldsymbol{x} + \boldsymbol{c}_i, t+1) = \boldsymbol{g}^\star(\boldsymbol{x}, t) \tag{26}$$

through the space-time cylinder. The computing steps implemented in one collision are summarized in Algorithm 1 and the streaming is realized as a mere pointer shift [21]. The present work illustrates only the bulk solver.

Standard LBM boundary methods are applied to impose velocity boundary conditions for the binary fluid. The macroscopic initial conditions are implemented via initialization of the populations to the corresponding equilibrium and alignment of kinetic moments through collisions [25] preceding the actual simulation time horizon.

Algorithm 1 FRE LBM bulk collision kernel

procedure COLLIDE($\boldsymbol{f}$) ▷ Input: pre-collision $\boldsymbol{f}$ and $\boldsymbol{g}$ at local node $(\boldsymbol{x}, t)$
  compute zeroth moments:
    mixture density $\rho \leftarrow \sum_i f_i$ ▷ (10)
    order parameter $\phi \leftarrow \sum_i g_i$ ▷ (20)
  compute potentials: $\mu_\rho \leftarrow (\rho, \phi)$ and $\mu_\phi \leftarrow (\rho, \phi)$ ▷ (17), (18)
  compute forcing, via:
    force $\boldsymbol{F} \leftarrow (\rho, \mu_\rho, \phi, \mu_\phi)$ ▷ (13)
    velocity $\boldsymbol{u} \leftarrow (\boldsymbol{f}, \rho, \boldsymbol{F})$ ▷ (11)
    force term $\boldsymbol{S} \leftarrow (\boldsymbol{u}, \boldsymbol{F})$ ▷ (9)
  compute equilibria: $\boldsymbol{f}^{\mathrm{eq}} \leftarrow (\rho, \boldsymbol{u})$ and $\boldsymbol{g}^{\mathrm{eq}} \leftarrow (\phi, \mu_\phi, \boldsymbol{u})$ ▷ (8) , (22)
  local collision of $\boldsymbol{f}^\star \leftarrow (\boldsymbol{f}, \boldsymbol{f}^{\mathrm{eq}}, \boldsymbol{S})$ and $\boldsymbol{g}^\star \leftarrow (\boldsymbol{g}, \boldsymbol{g}^{\mathrm{eq}})$ ▷ (6), (21)
  return $\boldsymbol{f}^\star$, $\boldsymbol{g}^\star$
end procedure ▷ Output: post-collision $\boldsymbol{f}^\star$ and $\boldsymbol{g}^\star$ at local node $(\boldsymbol{x}, t)$

3. **Numerical results.** To assess the capability of the FRE LBM for recovering shear and extensional binary flows, we emulate Taylor's parallel-band and four-roller devices [39] by means of numerical simulations in two dimensions (2D). The former is also tested for three dimensions (3D). The geometric setup of the 2D simulations is sketched in Figure 2.

All computations are done with OpenLB release 1.4 [19] on several HPC machines, using for example 16 nodes with five quad-core Intel Xeon E5-2609v2 cores each, or up to 75 nodes with respectively two deca-core Intel Xeon E5-2660v3.

The deformation of the C_1 droplet

$$D = \frac{L - B}{L + B}, \tag{27}$$

where L is the longer axis halved and B the shorter one, is measured via intrinsic functors of OpenLB [18]. In case of a horizontally measured inclination angle $\theta = 0°$, an interpolation along the space directions recovers the location of the interface. If a simultaneous deformation and inclination of the droplet occurs, L and B are approximated through concentric circles and θ can be computed at the respective intersection points with the interface.

Though essential differences between 2D and 3D deformations are known [37], certain non-dimensional regimes still allow a side-by-side comparison. Based on that we compare the FRE LBM solutions to 3D reference computations [17, 24] and analytical predictions [28, 39].

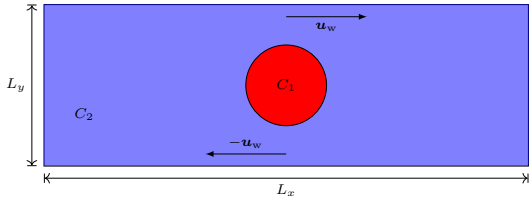

(A) Shear flow

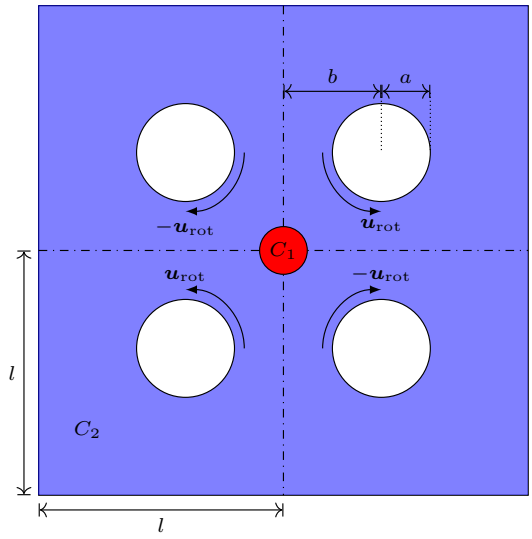

(B) Extensional flow

FIGURE 2. Geometric setup of numerical test cases for binary flow in two dimensions. Scales differ for the purpose of representation.

3.1. **Binary shear flow.** We define the non-dimensional Reynolds number, capillary number, Péclet number, and Cahn number, respectively as

$$Re = \frac{\gamma a^2 \rho}{\eta}, \tag{28}$$

$$Ca = \frac{a\gamma\mu_c}{\sigma}, \tag{29}$$

$$Pe = \frac{\gamma a \xi}{M_\phi A}, \tag{30}$$

$$Ch = \frac{\xi}{a}, \tag{31}$$

where γ, a, μ, σ, ξ are shear rate, droplet radius, viscosity, surface tension, interface thickness, respectively, and $A = 3\sigma/(2\xi)$ is a mobility parameter. The ratios of viscosity and density of the components are unity and time is understood as normalized via $\bar{t} = \gamma t$.

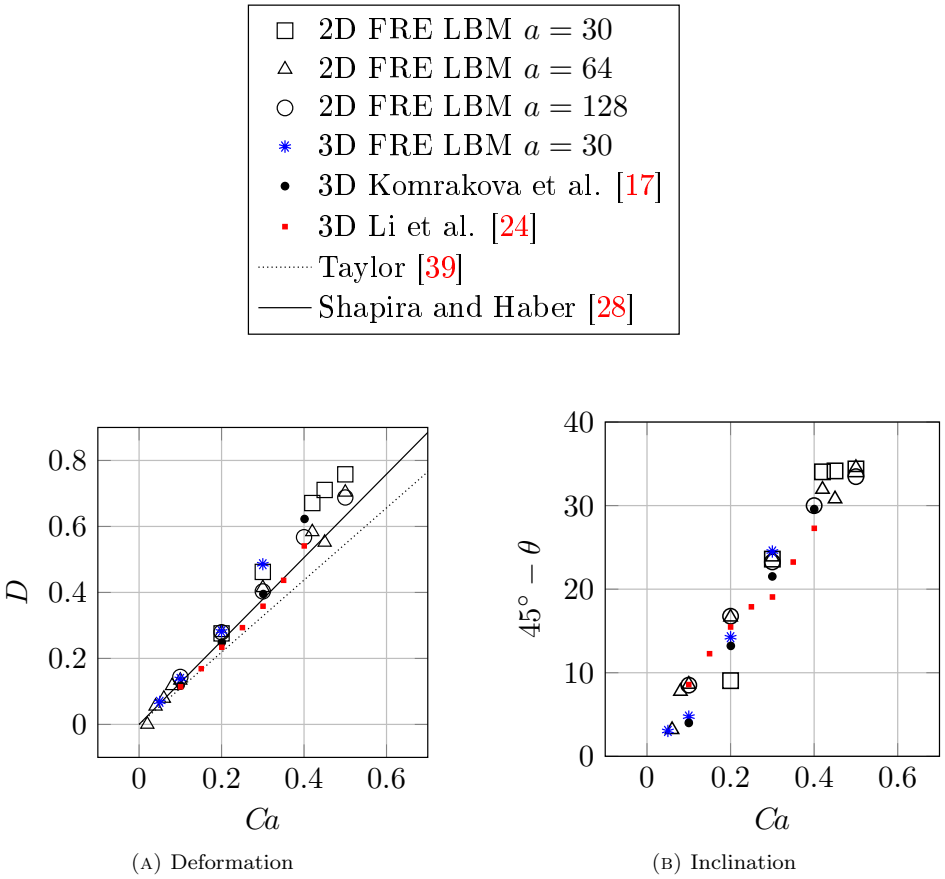

(A) Deformation (B) Inclination

FIGURE 3. Deformation and inclination of a droplet in binary shear flow simulated with FRE LBM for varying capillary numbers.

3.1.1. *Steady state validation.* In the case of $Ca < Ca_c$, the droplet deforms until it reaches a steady state. For $Re = 0.1$, $Pe = 0.43$, and $Ch = 0.0379$, Ca is varied over the interval $(0.02, 0.6)$. The results are plotted in Figure 3b and agree well with the literature for small Ca. Refining the mesh over several droplet radii in lattice units $a = 30, 64, 128$, indicates convergence to the reference results and allows to simulate validly for higher Ca. Notably, in the transition regime towards Ca_c, the droplet tilts and deforms towards an elongated thread and falls back into the stationary shape. This physical effect leads to an increased difference in results for lower grid resolutions.

3.1.2. *Breakup.* The first breakup occurs for $a = 30$ approximately at $Ca_c \approx 0.7$ (2D) and $Ca_c \approx 0.42$ (3D). Three different categories are known [3, 43], namely

(i) pseudo steady-state $Ca \lesssim Ca_c$,

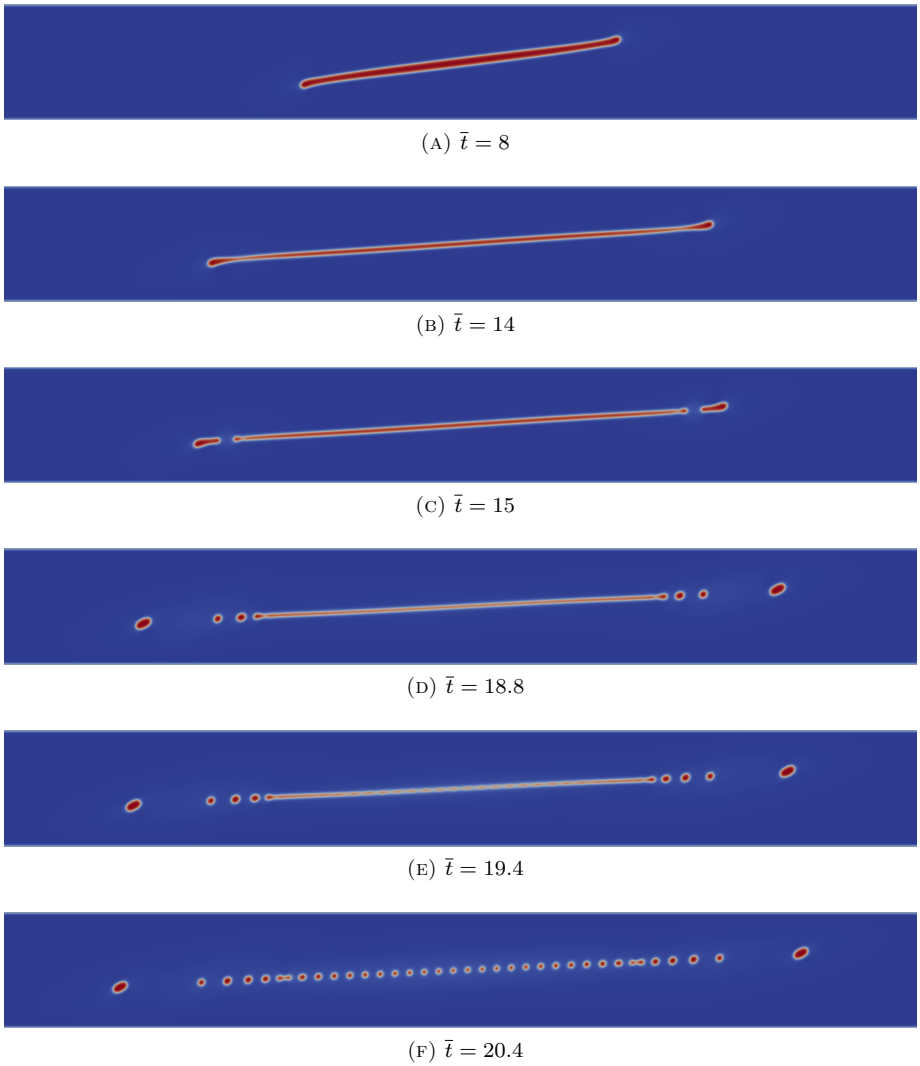

(A) $\bar{t} = 8$

(B) $\bar{t} = 14$

(C) $\bar{t} = 15$

(D) $\bar{t} = 18.8$

(E) $\bar{t} = 19.4$

(F) $\bar{t} = 20.4$

FIGURE 4. Droplet breakup in 2D binary shear flow at $Ca = 3.5$. Components C_1 (red) and C_2 (blue) are plotted at normalized time steps.

(ii) end-pinching $Ca_c \lesssim Ca \lesssim 2Ca_c$, and
(iii) capillary wave breakup $Ca \gtrsim 2Ca_c$.

The bounds between these regimes however are not sharp, such that the droplet may pass through multiple types during the breakup process. Due to differences between 2D and 3D droplet deformations, Ca_c in 2D is significantly larger than in 3D. The latter agrees well with the literature [17], and so does the breakup scenario (see Figure 5). In 2D for $Ca = 5Ca_c$ at $Re = 1$, $Pe = 0.2$ and $a = 40$ we observe end-pinching as well as a capillary wave breakup (see Figure 4).

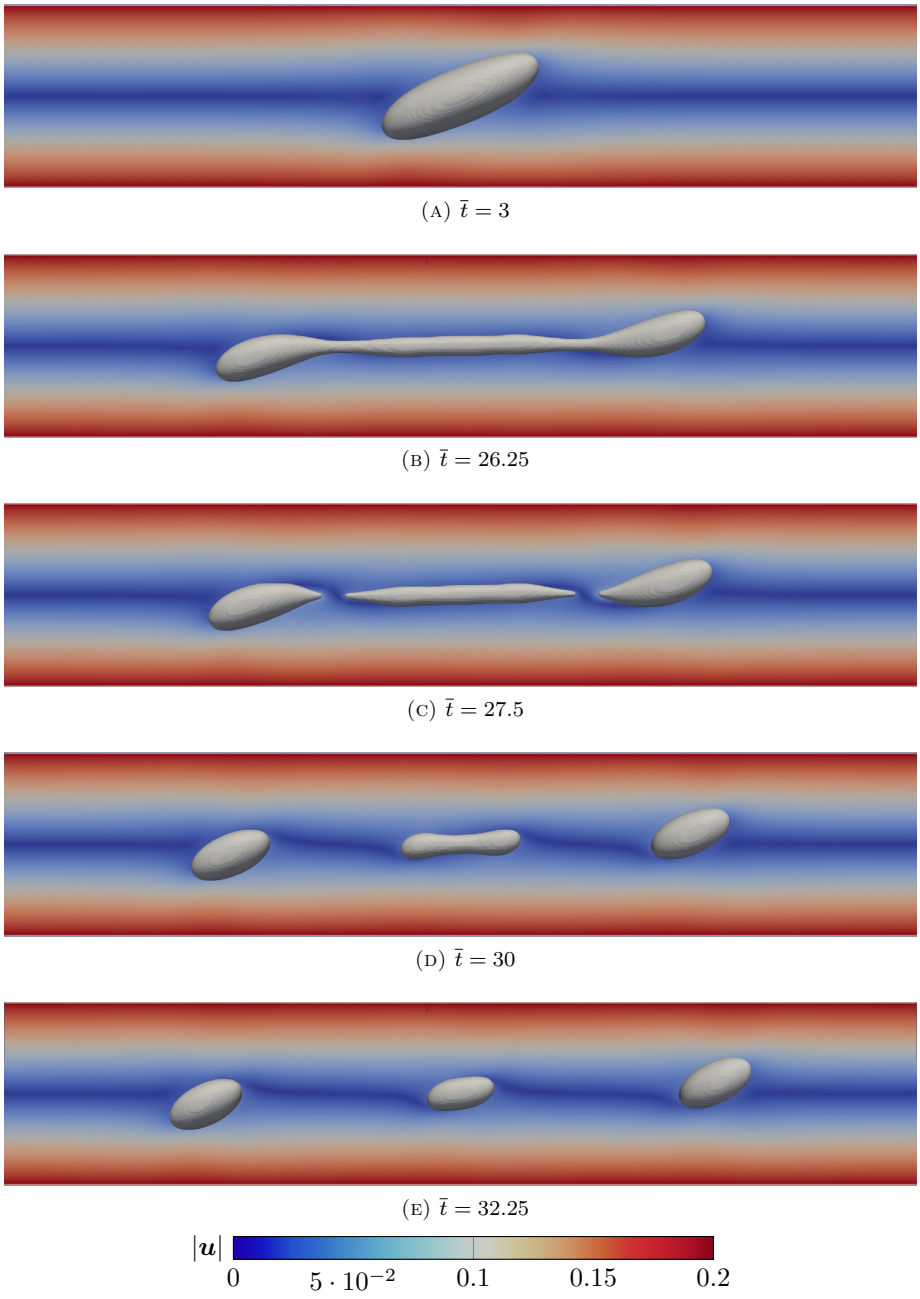

FIGURE 5. Droplet breakup in 3D binary shear flow at normalized time steps for $Re = 0.0625$, $Ca = 0.42$, $Ch = 0.0379$, $Pe = 0.43$.

3.2. **Binary extensional flow.** The sizing of the four-roller device ensures a uniform extension rate ϵ [11] which now replaces γ [12, 40, 1] in the π-group. For fixed

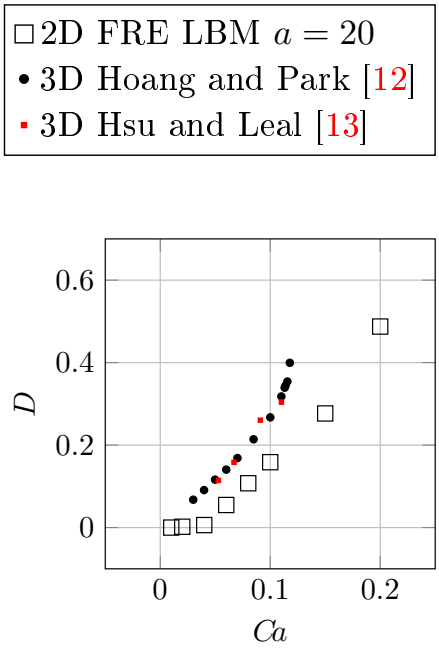

FIGURE 6. Deformation of a droplet in binary extensional flow simulated with FRE LBM for varying capillary numbers.

$Re = 0.0625$, $Ch = 0.57$, $Pe = 0.1$ and $Ca \in [0.01, 0.3]$ the droplet is observed to break for $Ca > 0.25$.

3.2.1. *Steady state validation.* The droplet radius is set to $a = 20$, which corresponds to a ratio of 40 between domain length and radius. Figure 6 summarizes the deformation in the subcritical capillary regime. For $Ca = 0.01, 0.02, 0.04$ the droplet shows little to no deformation. Beginning at $Ca = 0.05$ the deformation becomes significant and increases rapidly with increasing Ca and with a considerably faster rate than in the shear flow. Our simulation results and the reference data from [12, 13] agree from the perspective of an overall trend but differ at individual values. Based on the same reasoning as above, we conclude that a 3D extensional flow produces a higher deformation at lower Ca than in 2D.

3.2.2. *Breakup.* Figure 7 visualizes a breakup for $Ca = 0.42$. At first, the droplet stretches into a long thread of equal width with rounded ends. Instead of end-pinching, the droplet breaks by overstretching, forming several sub-satellite droplets. After the droplets exceed the rollers' gap, their velocity declines and the tails retract quickly. Despite the successful reproduction of these phenomena, the results show heavy satellite shrinkage due to the high domain-droplet ratio. The apparent shrinkage of sub-critical droplets is further discussed in Appendix A.

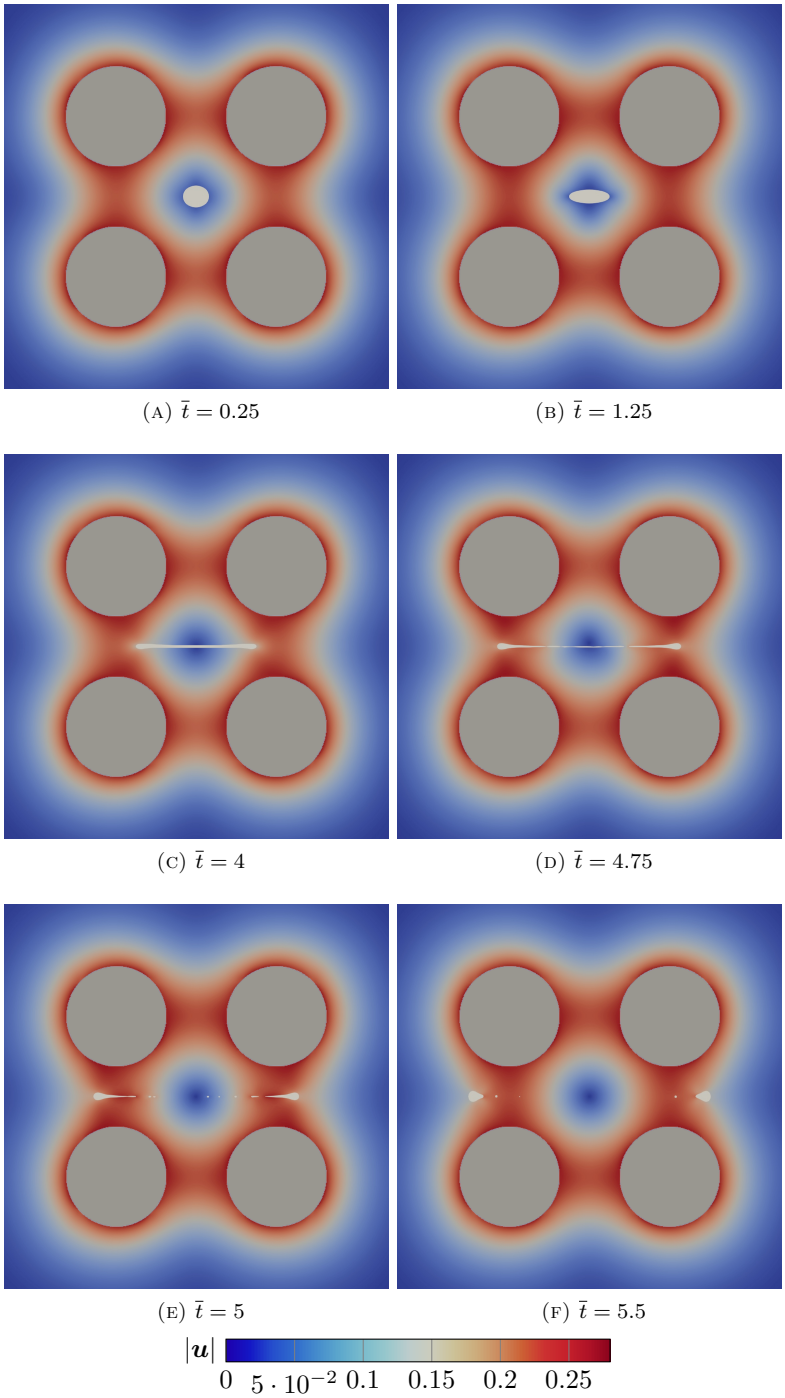

(A) $\bar{t} = 0.25$ (B) $\bar{t} = 1.25$

(C) $\bar{t} = 4$ (D) $\bar{t} = 4.75$

(E) $\bar{t} = 5$ (F) $\bar{t} = 5.5$

FIGURE 7. Droplet breakup in 2D binary extensional flow at normalized time steps for $Re = 0.0625$, $Ca = 0.42$, $Ch = 0.057$, $Pe = 0.43$.

4. **Conclusion.** We set up a FRE LBM algorithm implementation in OpenLB and test it for shear and extensional binary fluid flow in two and three dimensions. Taylor's parallel-band and four-roller devices are digitally twinned in a simplified manner and used for validation of the numerical scheme. To the authors' knowledge, the present work is the first application of LBM for simulating a four-roller apparatus. Characteristic deformations for steady states and breakup scenarios in critical capillary regimes are captured. Though the known satellite loss for very small droplet-domain ratios is observed, with suitably fine meshes we find good agreement to references.

To push forward the FRE LBM application in industrial processes, future studies should include model extensions to non-uniform viscosity and density ratios as well as conservative formulations and discretizations.

Acknowledgments. The authors thank Halim Kusumaatmaja for valuable discussions. S.S. thanks Taehun Lee for pointing out essential references. The authors acknowledge support by the state of Baden-Württemberg through bwHPC. Parts of this work were performed on the supercomputers ForHLR II and HoreKa funded by the Ministry of Science, Research and the Arts Baden-Württemberg and by the Federal Ministry of Education and Research.

Author contributions. Conceptualization: **S.S.**; Software: **S.S.**, **J.N.**, **S.J.A.**, **M.J.K.**; Methodology: **S.S.**, **J.N.**, **S.J.A.**; Validation: **S.S.**, **J.N.**; Formal analysis: **S.S.**, **J.N.**; Investigation: **S.S.**, **J.N.**; Data Curation: **S.S.**, **J.N.**; Writing - Original draft: **S.S.**; Visualization: **S.S.**, **J.N.**; Supervision: **S.S.**; Project administration: **S.S.**; Writing - Review & Editing: **S.S.**, **J.N.**, **S.J.A.**, **W.D.**, **M.J.K.**; Resources: **M.J.K.**; Funding acquisition: **S.S.**, **M.J.K.**. All authors read and approved the final manuscript.

Appendix A. **Mass leakage.** Zheng et al. [44] derived a formula for computing the critical value for an initial droplet radius such that any smaller droplet will disappear in a FRE LBM multiphase flow simulation. Though the results are derived for liquid-vapor systems with a different free energy functional, the fundamental FRE derivation and the CHE is similar to our approach. Previous results, relating the spontaneous drop shrinkage to the interface thickness, have been obtained for phase-field finite-element simulations by Yue et al. [42]. The source of leakage is identified therein as follows. The requirement of $\phi = \pm 1$ in the bulk essentially depends on the interface having negligible volume compared to the bulk so that solely the bulk free energy (non-gradient terms in brackets of (14)) matters in the energy minimization. For non-planar interfaces as apparent here (see Figure 2), this is analytically not the case. Hence, the free energy is concentrated on the interface. Due to the bulk volume being finite, the total energy can be reduced by shifting the initial values of ϕ and shrinking the drop at the same time (cf. [42, Figure 1]). As such, the volume loss is a fundamental mechanism inherent to free energy dynamics governed by the CHE. It can however be reduced to an acceptable amount by careful parameter selection or advanced discretization, which both have to ensure a very small ratio of interface width to drop volume or equivalently $C\!h \ll 1$. Depending additionally on the volume of the initial drop and the volume of the computational domain, a relative critical radius a_c can be derived [42, 44]. Based on that, if the ratio of critical and initial drop radius exceeds unity ($a_\mathrm{c}/a_0 > 1$), the drop will shrink and eventually disappear [44]. The derivation of such a bound

for the present FRE LBM is deferred to future studies. It is however left to be noted that the suggested bound on the Cahn number ($Ch \lesssim 0.01$) [42] has been found suitable also for our purposes. We ascribe the validity of this bound to the observation that in the incompressible limit we may express the Landau free energy [20] as a special case of the present one.

Possible solution approaches which modify only the FRE to delay the droplet shrinkage at large Ch to later timesteps have been proposed recently by Shin et al. [29]. As a first step towards reducing the droplet shrinkage in the present FRE LBM, we adapt the methodology from [29]. We refer to the non-gradient terms in (14) as $h^{(m)}(\rho,\phi)$ where $m=2$ and rewrite the free energy functional as

$$\Psi^{(m)} = \int_\Omega \left[h^{(m)}(\rho,\phi) + \frac{\alpha^2\kappa_1}{8}(\boldsymbol{\nabla}\rho + \boldsymbol{\nabla}\phi)^2 + \frac{\alpha^2\kappa_2}{8}(\boldsymbol{\nabla}\rho - \boldsymbol{\nabla}\phi)^2 \right] \mathrm{d}\boldsymbol{x}. \tag{32}$$

Setting $\kappa := \kappa_1 = \kappa_2$, we obtain

$$h^{(m)}(\rho,\phi) = \frac{\kappa}{16}\left[(\phi^m + 3\rho^2 - 6\rho + 2)^2 - (3\rho^2 - 6\rho + 2)^2 + \rho^4 - 4\rho^3 + 4\rho^2\right]. \tag{33}$$

Taking the formal non-dimensional incompressible limit, (33) becomes

$$\lim_{\rho\to 1} h^{(m)}(\rho,\phi) = \frac{\kappa}{16}(\phi^m - 1)^2 =: \tilde{h}^{(m)}(\phi). \tag{34}$$

It is to be noted that the derivation in [29] is carried out for the limit free energy $\tilde{h}^{(m)}$ with $\kappa = 4$ in (34) only. Therein [29], a higher-order free energy polynomial setting $m > 2$ counteracts the vanishing sub-critical sized droplets via penalizing the steepness near the minima of the double-well potential. Conclusively, a positive recommendation is given towards $m = 6$, while $m \gg 6$ results in non-physical effects on the interface shape. To investigate the effects of the higher order polynomial

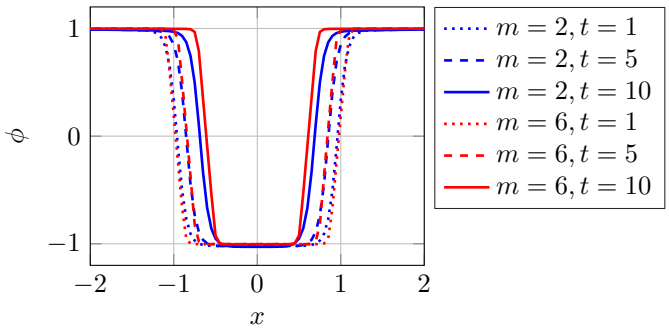

FIGURE 8. Static droplet test case in 2D computed with FRE LBM. The order parameter ϕ is plotted over the cross section $y = 0$ for the free energy functional $\Psi^{(m)}$ with $m = 2$ and $m = 6$ at several time steps.

for the present FRE LBM, the modified $\Psi^{(6)}$ is evaluated against the standard $\Psi = \Psi^{(2)}$ in a static 2D test case where a circular droplet ($\phi = 1$) is immersed in a quadratic domain filled with the other component ($\phi = -1$). The velocity field and the external forces are nulled out. The droplet has a radius of $a = 20$ with an interface thickness $\xi = 2.27$ which results in $Ch = 0.1135$ and thus is prone to strong shrinkage. Figure 8 visualizes the cross section of ϕ at different

time steps. In the case of $m = 2$, we observe that the order parameter reaches a shifted value of $\phi \approx -1.027$ at the center of the droplet, as well as a decreased value in the surrounding fluid region. This observation agrees well with results from Komrakova et al. [17] who identified the so-called contamination to be caused by residual diffusion of the interface. It is to be stressed that, though the higher order polynomial with $m = 6$ corrects the unwanted shift from the local minima and prevents the contamination, the shrinkage of the droplet is still present and seems to even be increased for larger times. We thus postpone further investigations and model development to future studies and presently use $m = 2$ throughout the paper.

REFERENCES

[1] B. J. Bentley and L. G. Leal, An experimental investigation of drop deformation and breakup in steady, two-dimensional linear flows, *Journal of Fluid Mechanics*, **167** (1986), 241-283.

[2] P. L. Bhatnagar, E. P. Gross and M. Krook, A model for collision processes in gases. I. small amplitude processes in charged and neutral one-component systems, *Physical Review E*, **94** (1954), 511-525.

[3] D. I. Bigio, C. R. Marks and R. V. Calabrese, Predicting drop breakup in complex flows from model flow experiments, *International Polymer Processing*, **13** (1998), 192-198.

[4] F. Bukreev, S. Simonis, A. Kummerländer, J. Jeßberger and M. J. Krause, Consistent lattice Boltzmann methods for the volume averaged Navier–Stokes equations, preprint, `arXiv:2208.09267`, 2022.

[5] S. G. K. Calhoun, K. K. Brower, V. C. Suja, G. Kim, N. Wang, A. L. McCully, H. Kusumaatmaja, G. G. Fuller and P. M. Fordyce, Systematic characterization of effect of flow rates and buffer compositions on double emulsion droplet volumes and stability, *Lab on a Chip*, **22** (2022), 2315-2330.

[6] M. E. Cates and E. Tjhung, Theories of binary fluid mixtures: From phase-separation kinetics to active emulsions, *Journal of Fluid Mechanics*, **836** (2018), 68 pp.

[7] D. Dapelo, S. Simonis, M. J. Krause and J. Bridgeman, Lattice-Boltzmann coupled models for advection-diffusion flow on a wide range of Péclet numbers, *J. Comput. Sci.*, **51** (2021), 101363, 14 pp.

[8] Z. Guo, C. Zheng and B. Shi, Discrete lattice effects on the forcing term in the lattice Boltzmann method, *Physical Review E*, **65** (2002), 046308.

[9] M. Haussmann, P. Reinshaus, S. Simonis, H. Nirschl and M. J. Krause, Fluid–structure interaction simulation of a coriolis mass flowmeter using a lattice Boltzmann method, *Fluids*, **6** (2021), 167.

[10] M. Haussmann, S. Simonis, H. Nirschl and M. J. Krause, Direct numerical simulation of decaying homogeneous isotropic turbulence – numerical experiments on stability, consistency and accuracy of distinct lattice Boltzmann methods, *Internat. J. Modern Phys. C*, **30** (2019), 1-29.

[11] J. J. L. Higdon, The kinematics of the four-roll mill, *Physics of Fluids A*, **5** (1993), 274-276.

[12] V. T. Hoang and J. M. Park, A Taylor analogy model for droplet dynamics in planar extensional flow, *Chemical Engineering Science*, **204** (2019), 27-34.

[13] A. S. Hsu and L. G. Leal, Deformation of a viscoelastic drop in planar extensional flows of a Newtonian fluid, *J. Non-Newton. Fluid Mech.*, **160** (2009), 176-180.

[14] H. Huang, M. Sukop and X. Lu, *Multiphase Lattice Boltzmann Methods: Theory and Application*, John Wiley & Sons, 2015.

[15] V. M. Kendon, M. E. Cates, I. Pagonabarraga, J.-C. Desplat and P. Bladon, Inertial effects in three-dimensional spinodal decomposition of a symmetric binary fluid mixture: A lattice Boltzmann study, *Journal of Fluid Mechanics*, **440** (2001), 147-203.

[16] J. Kim, Phase field computations for ternary fluid flows, *Comput. Methods Appl. Mech. Engrg.*, **196** (2007), 4779-4788.

[17] A. E. Komrakova, O. Shardt, D. Eskin and J. J. Derksen, Lattice Boltzmann simulations of drop deformation and breakup in shear flow, *International Journal of Multiphase Flow*, **59** (2014), 24-43.

[18] M. J. Krause, A. Kummerländer, S. J. Avis, H. Kusumaatmaja, D. Dapelo, F. Klemens, M. Gaedtke, N. Hafen, A. Mink, R. Trunk, J. E. Marquardt, M.-L. Maier, M. Haussmann

and S. Simonis, OpenLB—Open source lattice Boltzmann code, *Comput. Math. Appl.*, **81** (2021), 258-288.
[19] M. J. Krause, S. Avis, H. Kusumaatmaja, D. Dapelo, M. Gaedtke, N. Hafen, M. Haußmann, Jonathan Jeppener-Haltenhoff, L. Kronberg, A. Kummerländer, J.E. Marquardt, T. Pertzel, S. Simonis, R. Trunk, M. Wu and A. Zarth, OpenLB Release 1.4: Open Source Lattice Boltzmann Code, *Zenodo*, (2020).
[20] T. Krüger, H. Kusumaatmaja, A. Kuzmin, O. Shardt, G. Silva and E. M. Viggen, *The Lattice Boltzmann Method: Principles and Practice*, Springer International Publishing, 2017.
[21] A. Kummerländer, M. Dorn, M. Frank and M. J. Krause, Implicit propagation of directly addressed grids in lattice Boltzmann methods, *Concurrency and Computation*, (2021), e7509.
[22] H. Kusumaatmaja and J. M. Yeomans, Lattice Boltzmann simulations of wetting and drop dynamics, *Simulating Complex Systems by Cellular Automata*, (2010), 241-274.
[23] P. Lallemand, L.-S. Luo, M. Krafczyk and W.-A. Yong, The lattice Boltzmann method for nearly incompressible flows, *J. Comput. Phys.*, **431** (2021), 109713, 52 pp.
[24] J. Li, Y. Y. Renardy and M. Renardy, Numerical simulation of breakup of a viscous drop in simple shear flow through a volume-of-fluid method, *Physics of Fluids*, **12** (2000), 269-282.
[25] R. Mei, L.-S. Luo, P. Lallemand and D. d'Humières, Consistent initial conditions for lattice Boltzmann simulations, *Computers and Fluids*, **35** (2006), 855-862.
[26] A. Mink, K. Schediwy, C. Posten, H. Nirschl, S. Simonis and M. J. Krause, Comprehensive computational model for coupled fluid flow, mass transfer, and light supply in tubular photobioreactors equipped with glass sponges, *Energies*, **15** (2022).
[27] C. Semprebon, T. Krüger and H. Kusumaatmaja, Ternary free-energy lattice Boltzmann model with tunable surface tensions and contact angles, *Physical Review E*, **93** (2016), 033305.
[28] M. Shapira and S. Haber, Low Reynolds number motion of a droplet in shear flow including wall effects, *Int. J. Multiphase Flow*, **16** (1990), 305-321.
[29] J. Shin, J. Yang, C. Lee and J. Kim, The Navier-Stokes-Cahn-Hilliard model with a high-order polynomial free energy, *Acta Mechanica*, **231** (2020), 2425-2437.
[30] S. Simonis, M. Frank and M. J. Krause, On relaxation systems and their relation to discrete velocity Boltzmann models for scalar advection–diffusion equations, *Philos. Trans. Roy. Soc. A*, **378** (2020), 20190400, 16 pp.
[31] S. Simonis, M. Frank and M. J. Krause, Constructing relaxation systems for lattice Boltzmann methods, *Applied Mathematics Letters*, **137** (2023), 108484.
[32] S. Simonis, M. Haussmann, L. Kronberg, W. Dörfler and M. J. Krause, Linear and brute force stability of orthogonal moment multiple-relaxation-time lattice Boltzmann methods applied to homogeneous isotropic turbulence, *Philos. Trans. Roy. Soc. A*, **379** (2021), 20200405, 19 pp.
[33] S. Simonis and M. J. Krause, Forschungsnahe lehre unter Pandemiebedingungen, *Mitteilungen der Deutschen Mathematiker-Vereinigung*, **30** (2022), 43-45.
[34] S. Simonis and M. J. Krause, Limit consistency for lattice Boltzmann equations, preprint, `arXiv:2208.06867`, 2022.
[35] S. Simonis, D. Oberle, M. Gaedtke, P. Jenny and M. J. Krause, Temporal large eddy simulation with lattice Boltzmann methods, *J. Comput. Phys.*, **454** (2022), 110991, 19 pp.
[36] M. Siodlaczek, M. Gaedtke, S. Simonis, M. Schweiker, N. Homma and M. J. Krause, Numerical evaluation of thermal comfort using a large eddy lattice Boltzmann method, *Building and Environment*, **192** (2021), 107618.
[37] G. Soligo, A. Roccon and A. Soldati, Deformation of clean and surfactant-laden droplets in shear flow, *Meccanica*, **55** (2020), 371-386.
[38] M. R. Swift, E. Orlandini, W. R. Osborn and J. M. Yeomans, Lattice Boltzmann simulations of liquid-gas and binary fluid systems, *Physical Review E*, **54** (1996), 5041.
[39] G. I. Taylor, The formation of emulsions in definable fields of flow, *Proc. R. Soc. Lond. A*, **146** (1934), 501-523.
[40] D. C. Tretheway and L. G. Leal, Deformation and relaxation of Newtonian drops in planar extensional flows of a Boger fluid, *J. Non-Newton. Fluid Mech.*, **99** (2001), 81-108.
[41] N. Wang, C. Semprebon, H. Liu, C. Zhang and H. Kusumaatmaja, Modelling double emulsion formation in planar flow-focusing microchannels, *Journal of Fluid Mechanics*, **895** (2020), 36 pp.
[42] P. Yue, C. Zhou and J. J. Feng, Spontaneous shrinkage of drops and mass conservation in phase-field simulations, *J. Comput. Phys.*, **223** (2007), 1-9.

[43] X. Zhao, Drop breakup in dilute Newtonian emulsions in simple shear flow: New drop breakup mechanisms, *Journal of Rheology*, **51** (2007), 367-392.
[44] L. Zheng, T. Lee, Z. Guo and D. Rumschitzki, Shrinkage of bubbles and drops in the lattice Boltzmann equation method for nonideal gases, *Physical Review E*, **89** (2014), 033302.

Received December 2022; revised February 2023; early access March 2023.